LA-UR-20-23286

Title: Thermal interfaces in dynamic compression experiments

Author(s):
Hartsfield, Thomas Murray
LaLone, Brandon M.
Stevens, Gerald D.
Veeser, Lynn R.
Dolan, Daniel H.

Intended for: Journal of Applied Physics

Issued: 2020-04-30 (Draft)

Journal of Applied Physics
DOE/NV/03624--0790

Thermal interfaces in dynamic compression experiments

T.M. Hartsfield,[1] B.M. LaLone,[2] G.D. Stevens,[2] L.R. Veeser,[2] and D.H. Dolan[3]
[1] *Group P-23, Los Alamos National Laboratory, Los Alamos, New Mexico 87545, USA*[a]
[2] *Nevada National Security Site, Special Technologies Laboratory, Santa Barbara, California 93111, USA*
[3] *Sandia National Laboratories, Albuquerque, New Mexico 87185, USA*[b]

(Dated: 1 June 2020)

Temperature is a difficult thermodynamic variable to measure in dynamic compression experiments. Optical pyrometry is a general-purpose technique for measuring temperature from a radiant surface, but that surface is often the interface between distinct materials with temperatures that vary spatially along the loading direction. This leads to a fundamental problem: how does measured interface temperature relate to this temperature profile along the compression axis? Numerical analysis of loading history and thermal diffusion at these interfaces show that seemingly subtle changes in experiment geometry can lead to very different temperature profiles. We compare these results to laboratory temperature measurements of shock-compressed tin.

I. BACKGROUND

Time-resolved temperature measurements are critical to equation of state, phase transition, and chemical reaction research using dynamic compression.[1] Optical pyrometry[2–4] measures the radiant flux (within a spectral band) from a surface with a given emissivity and solves the Planck function to infer temperature of the radiant surface. The technique is applicable to all radiant surfaces, but is limited in implementation by several difficulties. Practical issues include precise radiometry technique (*e.g.*, choice of proper measurement wavelengths[5]), elimination of non-thermal optical background sources,[6] and constraining spectral emissivity.[7–11] Properly addressing these issues produces a reliable time history of temperature at a radiating surface.

There are three general classes of optical pyrometry in dynamic compression research.

- Experiments where an initially transparent material (*e.g.*, quartz) is shocked to opacity.[2,12–14] Optical emission behind the shock front passes through the unshocked material. Measurement interpretation is usually straightforward,[15] but the technique is unsuitable for metals and other opaque materials.

- Experiments where an opaque material is compressed and its free surface allowed to unload into a gas or vacuum atmosphere.[16–20] In principle, this interface makes for simple temperature interpretation, but unloaded free surfaces are prone to fragmentation. Spall, cavitation, jetting, and/or fine particulate ejecta can create complex distributions of material composition and temperature.

- Experiments where an opaque sample is compressed by shock or ramp wave against a transparent window.[4,21,22] Sample emission passes through this optical window connected to the sample, while the window itself remains transparent under compression.

The third class of experiment simplifies field-of-view composition and uniformity, but involves one or more material interfaces that make interpretation challenging. Figure 1 illustrates the material interfaces present for optical thermometry of an opaque sample. An optical window must be in mechanical contact with the sample to maintain non-zero stress at the emitting-reflecting surface, so there is always at least one material interface. In practice, an intermediate layer (glue/epoxy) attaches the window to the sample, creating two interfaces. A related dual-interface example is direct impact (sometimes called "reverse-impact," or "reverse ballistic impact") of a sample onto a window coated with an opaque emissive film.

There is a fundamental disconnect between the measured interface temperature and the bulk temperature of interest. An obvious consequence of optical window attachment is mechanical impedance mismatch: the interface undergoes a release or recompression, so the measured state differs from the original sample compression state. Such changes are well understood, and the release/reshock state is observed by optical velocimetry.[23,24] More subtle, but nevertheless significant, discrepancies between measured temperature and mechanical state (stress, particle velocity, etc.) occur at material interfaces. Stress gradients lead to wave propagation at km/s speeds; temperature differences lead to localized diffusion.

The following sections consider temperature issues for single-interface and two-interface experiments. Thermal diffusion is a recurring theme, building on concepts introduced by Urtiew and Grover.[25,26] Finite thermal conduction through the sample interface can dictate the diffusion process, and localized mechanical effects determine the initial material state in two-interface experiments. Two geometries—transmitted-shock and direct-impact—

---

[a] Electronic mail: hartsfield@lanl.gov
[b] Electronic mail: dhdolan@sandia.gov

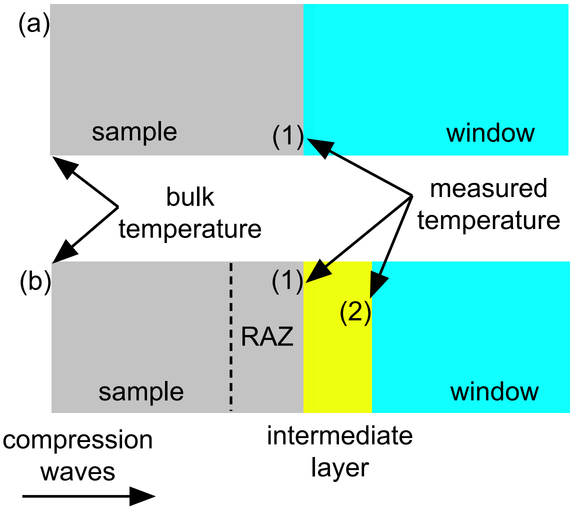

FIG. 1. (a) Dynamic temperature measurement with one material interface. (b) Dynamic temperature measurement with two material interfaces, where radiance might be collected from the front (1) or back (2) of the intermediate layer. This layer creates a reverberation-affected-zone (RAZ) layer at the sample interface.

TABLE I. Characteristic thermal properties for metals, ordered insulators, and polymers.

	ρ (g cm^{-3})	c_P (J g^{-1} K^{-1})	k_T (W m^{-1} K^{-1})	κ (m^2 s^{-1})
Metals	2–22	0.1-1	10–400	10^{-4}–10^{-5}
Insulators	2–7	$\sim$1	1–50	10^{-5}–10^{-6}
Polymers	$\sim$1	$\sim$1	0.1–1	10^{-6}–10^{-7}

are considered in detail and compared with the results of pyrometry experiments.

Radiative cooling of the emissive surface is ignored throughout this discussion. Combining the Stefan-Boltzmann law with an analytic solution from Reference 27, one can show that radiative cooling is bounded by:

$$\frac{\Delta T}{T} \lesssim \frac{2}{\sqrt{\pi}} \frac{\sigma T^3}{E} \sqrt{\Delta t} \tag{1}$$

where $E \equiv \rho c_p k_T$ is a material's effusivity. At 1000 K, the fractional change in a Sn sample over 1000 ns is about 5×10^{-6}; the change at 2000 K is roughly 65×10^{-6}.

II. SINGLE-INTERFACE TEMPERATURES

Thermal diffusion time and length scales are linked to diffusivity:

$$\kappa \equiv \frac{k_T}{\rho c_p} = \frac{[\text{length}]^2}{[\text{time}]} \tag{2}$$

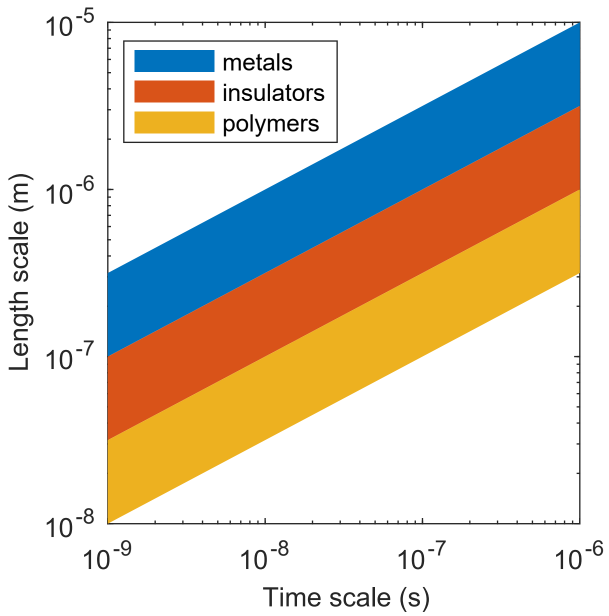

FIG. 2. Characteristic diffusion scales for metals, insulators, and amorphous materials

where k_T is the thermal conductivity, ρ is the density, and c_p is the isobaric specific heat. Table I lists characteristic parameters for fully dense (non-porous) materials. Thermal diffusivity varies significantly between material classes: 10^{-4} to 10^{-5} m^2/s for metals; 10^{-5} to 10^{-6} m^2/s for ordered insulators; and 10^{-6} to 10^{-7} m^2/s for polymers.[28,29] Figure 2 shows how diffusion length scales vary with time for each material class. For all but the best metals, thermal diffusion is limited to micron lengths over 100 ns time scales.

A. Theory

Thermal diffusion between two material layers can be simulated with the numerical method of lines.[30] Diffusion within each layer (sample A, window B) is linked to two boundary conditions at the interface $x = 0$.

$$k_A \frac{\partial T_A}{\partial x} = k_B \frac{\partial T_B}{\partial x} \tag{3}$$

$$T_B = T_A + \frac{k_A}{G} \frac{\partial T_A}{\partial x} \tag{4}$$

Interface conductance G accounts for the imperfect transfer of heat between materials. Heat flow through the interface requires a temperature discontinuity between the sample and window. Contact and boundary conductance both regulate heat flow through the interface.

$$\frac{1}{G} = \frac{1}{G_{Con}} + \frac{1}{G_{Bnd}} \tag{5}$$

Contact conductance describes the regulation of heat flow by microscale gaps between surfaces, the extent of

TABLE II. Material parameters for diffusion simulations

	ρ (g cm^{-3})	c_P (J g^{-1} K^{-1})	k_T (W m^{-1} K^{-1})	κ (m^2 s^{-1})
Sn	7.787†	0.213*	63	4.1×10^{-5}
LiF	2.64	1.92‡	10	2.0×10^{-6}
Glue	1.10	0.3	0.1	3.0×10^{-7}
Au	19.3	0.13	320	1.3×10^{-4}

* Manufacturer spec sheet (STP)
† Mabire
‡ Dulong-Petit limit

which depend strongly on roughness and longitudinal stress. For example, two copper plates clamped together at 10 MPa have contact conductance of $\sim 10^5$ W/(m^2·K); various theoretical models suggest G_{Con} is approximately linear in pressure.[31,32] Contact conductances of $\sim 10^8$ W/(m^2·K) are plausible for dynamic compression to $\sim$10 GPa.

Boundary conductance is related to the difficulty of transporting heat from one material to another, even for an atomically smooth interface.[33] Hot electrons in a metal, for example, cannot pass into a cold insulator, and vibrational coupling is hampered by differences in the phonon spectrum. Characteristic boundary conductances (at ambient conditions) are 10^7 to 10^{10} W/(m^2·K), slightly increasing with temperature and pressure.[34]

Figure 3 shows several numerical simulations of a Sn-LiF interface using parameters from Table II. For generality, temperatures are normalized between the bulk Sn and LiF temperatures. Infinite boundary conductance is approximated by $G = 10^{15}$ W/(m^2·K) for comparison with more plausible values. The assumption $G \to \infty$ is implicitly used in most discussion of shock temperature,[25,26] forcing continuous temperature at the interface with steeper gradients in the insulating window than the conducting sample. The normalized interface temperature can be determined analytically:[27]

$$T^* = \frac{E_A}{E_A + E_B} \tag{6}$$

where E_k is material effusivity $E \equiv \sqrt{k_T \rho c_P}$ for the sample (subscript "A") and window (subscript "B"). The interface temperature—0.58 in this example—is continuous across the interface, depending only upon the relative values of sample and window effusivity.

Interface conductances of 10^7 to 10^8 W/(m^2·K) lead to a noticeable temperature discontinuity at a Sn-LiF interface. Both cases suggest that temperatures measured immediately after shock compression can vary significantly from measurements taken 10–1000 ns later. Thermal diffusion is almost irrelevant on 1000 ns time scales for $G < 10^6$ W/(m^2·K) (not shown).

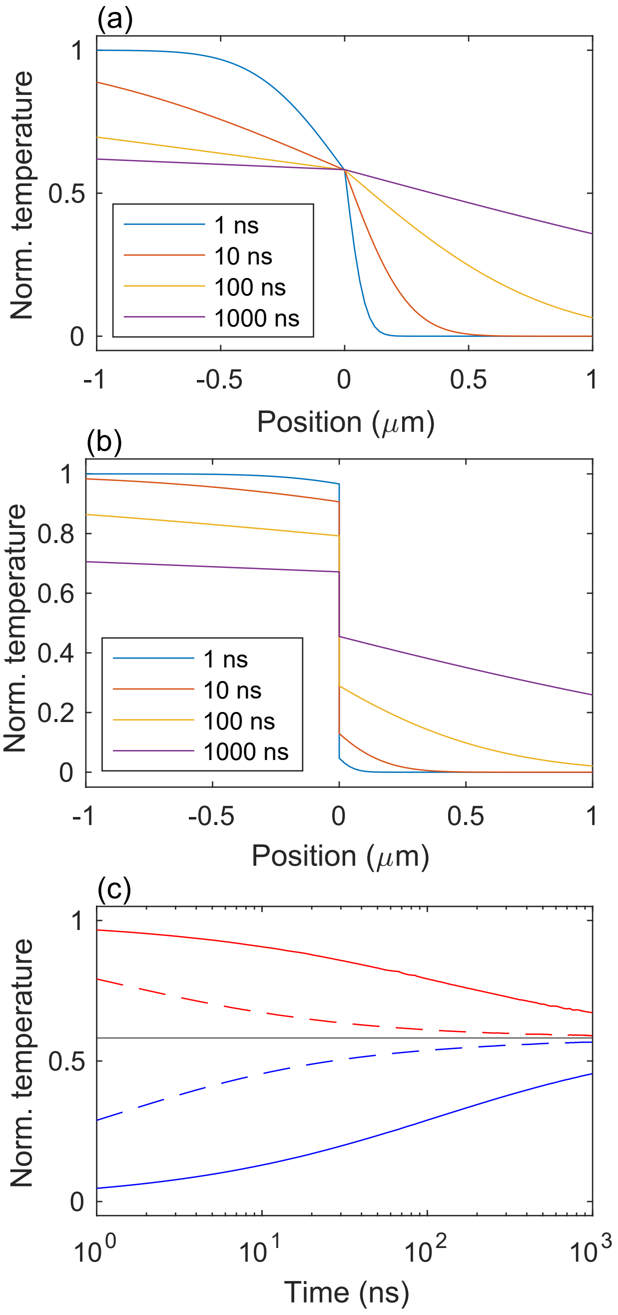

FIG. 3. Thermal diffusion simulations near a Sn-LiF interface. (a) Temperature snapshots with infinite interface conductance. (b) Temperature snapshots with finite interface conductance ($G = 10^7$ W/(m^2·K)). (c) Temperature history on the Sn (red lines) and LiF (blue lines) side of the interface. Solid lines are for $G = 10^7$ W/(m^2·K) and dashed lines for $G = 10^8$ W/(m^2·K).

B. Practical limitations

Perfect sample-window interfaces are conceptually appealing but difficult to achieve in practice. Clamping/pressing a sample to the window to eliminates the need for an intermediate adhesion layer, but temperature measurements in this configuration have so far been unsuccessful. In principle, direct launch of a sample onto to the window creates a single thermal interface, subject to finite boundary conductance described above, but residual gas trapped between the two surfaces becomes blinding for optical pyrometry measurements.[22]

An alternate approach has been reported for iron shock temperatures.[22,35] An impact-driven shock wave passes through a millimeter-scale iron sample and then a micron-scale iron coating deposited onto an optical window. The thick sample optically and thermally isolates the coating from much of the impact flash. In theory the sample is a perfect match to the coating, creating a single-interface pyrometry measurement; subsequent studies have highlighted possible interpretation issues with this data.[36–39] The primary difficulty is replicating bulk metal properties in the coating. Unpublished work using bonded Sn coatings on LiF have failed to produce sensible temperature measurements, presumably for similar reasons as iron:

- Density variations in the deposition of an inherently rough, polycrystalline coating layer.
- Dynamic void compaction that creates extraneous heat, contaminating the pyrometry measurement.
- Unavoidable surface oxidation, introducing layers of very different mechanical and thermal properties.

At best, the matched-coating approach is a two-interface problem—sample-coating and coating-window—because coatings are rarely identical to bulk material. Practical difficulties in creating thin-films on various substrates further limit the material composition and quality of coatings. Single-interface pyrometry may not be truly feasible in dynamic compression of opaque materials.

III. MULTIPLE-INTERFACE TEMPERATURES

Figure 4 shows two experiment configurations amenable to optical pyrometry: transmitted shock and modified direct-impact. Both geometries require the window to remain transparent, and thus non-emissive, over all pressures of interest. A number of window materials have been evaluated for pyrometry. Sapphire has been found to behave as a strong broadband emitter, beginning at a threshold beneath 20 GPa, depending upon crystal orientation.[40,41] Quartz becomes opaque at shock pressures of ∼6 GPa.[42] Diamond may remain transparent to 170 GPa,[43] but is impractical for most experiments. Unpublished studies have observed optical emission from MgO at pressures of 29 GPa. Temperatures in many of these materials are studied specifically by emission from transiting shock fronts..[14,44,45] Lithium fluoride is the standard window for these measurements. It can shock to pressures of 200 GPa, and ramp-compress to pressures in excess of 900 GPa without losing transparency.[4,14,40,46–49]

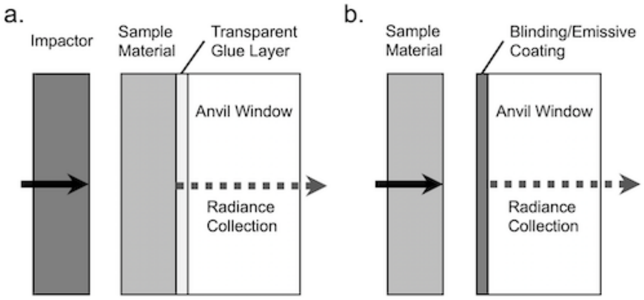

FIG. 4. Transmitted-shock (a) and direct-impact (b) experiment geometries

A. Transmitted-shock geometry

Transmitted-shock experiments use an impactor to create a high-pressure shock wave inside the (opaque) sample material, as shown in Figure 4(a). The optical window bonded to the back of the sample causes reshock or partial release (typically the latter) at shock breakout. This modification of sample pressure/temperature is not ideal, but the window preserves sample uniformity and prevents complete pressure release.

Optical windows are typically bonded to metal samples for optical pyrometry measurements.[4,21,22] The properties of this bond are critical: it must remain transparent over the pyrometer's spectral range during measurement; it must be free of voids, bubbles, or inconsistencies that will emit light under compression; and it must be applied in a very thin layer to minimize mechanical effects upon the dynamic loading path and to avoid possible light emission under compression in thicker layers. These requirements are challenging under static conditions and even more so under dynamic compression. Optical absorption in the bond attenuates sample light and emits unwanted light at its own temperature. The location and width of absorption features also change with compression, as will thin-film interference between the sample-bond and bond-window interfaces.

Few bond materials have been found to be suitable for visible and near-infrared pyrometry under shock compression. The single-component glue Loctite® 326, and its UV-cured analog Loctite® 358, can remain transparent to at least 55 GPa;[50] by 70 GPa there are signs of emission in micron-scale bonds of the former.[51] Epoxies commonly used in dynamic compression experiments—AngstromBond® and Stycast®—have been found in unpublished studies to emit enough light to hinder pyrometry. The details and mechanisms for these emission are not currently understood, but most glues and epoxies contain a multitude of mid-infrared absorptions (and their overtones) that presumably shift into the visible/near-infrared domain under compression. This does not explain why standard epoxies emit much more light than Loctite® 326—perhaps entrained bubbles from epoxy-hardener mixing play a role.

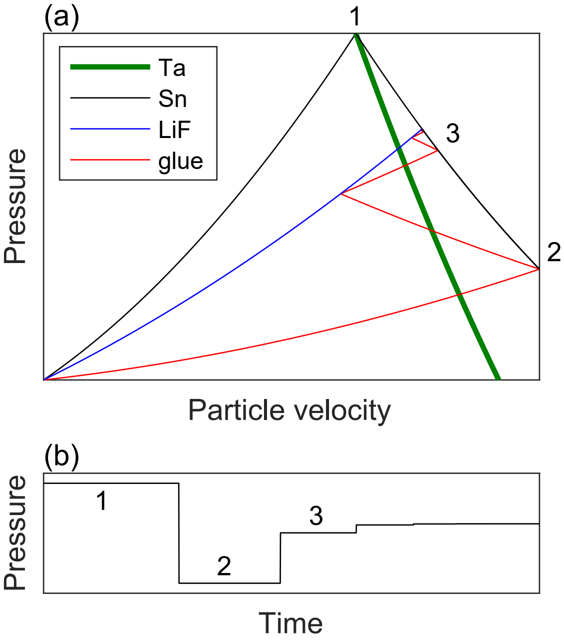

FIG. 5. (a) Calculated loading trajectory in a transmitted-shock experiment where Ta impacts Sn backed by LiF. The green line indicates Ta states, black lines indicate Sn states, the blue line indicates LiF states, and red lines indicate glue states. (b) Pressure history just inside the Sn sample. "1" represents the Sn shock pressure due to Ta impact, "2" the release of Sn into glue, "3" the reverberation of Sn interface and glue layer to Sn-LiF impedance match.

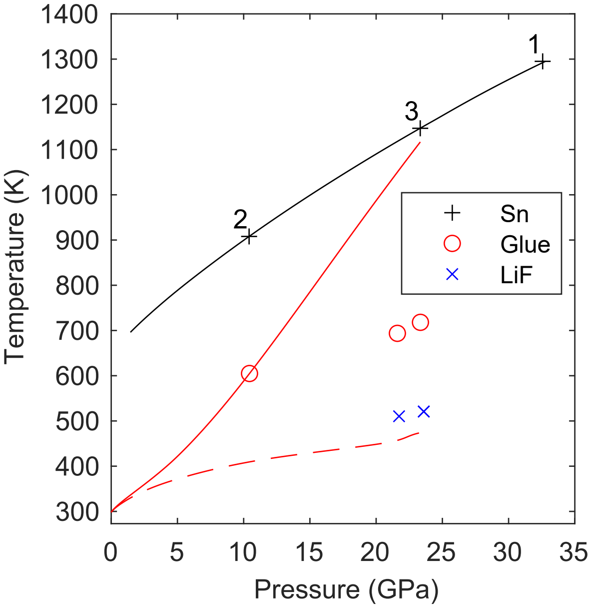

FIG. 6. Adiabatic temperature calculations for the transmitted-shock experiment in Figure 5. Black "+" markers indicate the initial shock (1), release (2), and reverberation (3) states of the Sn sample (Sesame 2160); the black curve is isentropic release from the initial shock state. Red "o" markers indicate glue temperature states (Sesame 7603); the solid red line are single-shock states and the dashed red line are isentropic states of glue, both starting from ambient conditions. Blue "x" markers indicate LiF states (Sesame 7270).

The bond layer changes sample loading from shock-release to shock-release-reverberation. Figure 5(a) illustrates pressure-particle velocity trajectories for the impact of Ta on Sn backed by LiF. The intersection of the left black curve with the green curve is the sample's initial shock state, while the intersection of the blue curve with the right black curve is release due to the LiF window. The bond layer, being lower impedance than either the sample or the window, undergoes reverberating shocks (red curves). Figure 5(b) illustrates pressure history just inside the Sn sample at the Sn-LiF interface. Sample emission originates from material shocked to a high pressure, released to a much lower pressure, then sequentially shocked to an intermediate pressure. This is (similar to a direct Sn-LiF impact).

A subtle benefit of bond reverberation is that the glue/epoxy layer is much cooler than single-shock compression to the same pressure. For example, the 1.558 km/s Ta impact shown in Figure 5 leads to a 23.3 GPa equilibrium between Sn and LiF. Most polymers decompose under 20–30 GPa shock compression,[52] but the glue layer in this example sees an initial shock of only 10.4 GPa. After reverberation, the glue layer is significantly cooler (720 K versus 1150 K) than a direct shock to the final state. Exact decomposition depends on the specific adhesive—and no formal models exist for the Loctite products mentioned above—but in all cases the bond layer will be cooler than in single-shock experiments. This presumably inhibits chemical reactions, allowing glue bonds to remain functional at higher pressures.

Figure 6 shows temperature-pressure estimates for all three material layers. When reverberation is complete:

- The sample has the highest temperature (1150 K) because it is exposed to the strongest (irreversible) shock. Metal samples also tend to have lower specific heat capacity than insulators and polymers.
- The glue has an intermediate temperature (720 K) arising from the high volume compression, mitigated by reverberation and moderate specific heat.
- The window has the lowest temperature (520 K) due to moderate volume compression and specific heat.

Only emission from the metal sample is significant to visible/near-infrared pyrometry.

The low diffusivity of glue (10^{-7} m^2/s) inhibits heat flow between the Sn sample and the LiF fluoride window. A 1 μm glue layer cannot equilibrate faster than 10 μs, so the window temperature is irrelevant to sample temperature for micron-scale bonding. The equilibrium temperature ratio at the Sn-glue interface (Equation 6)

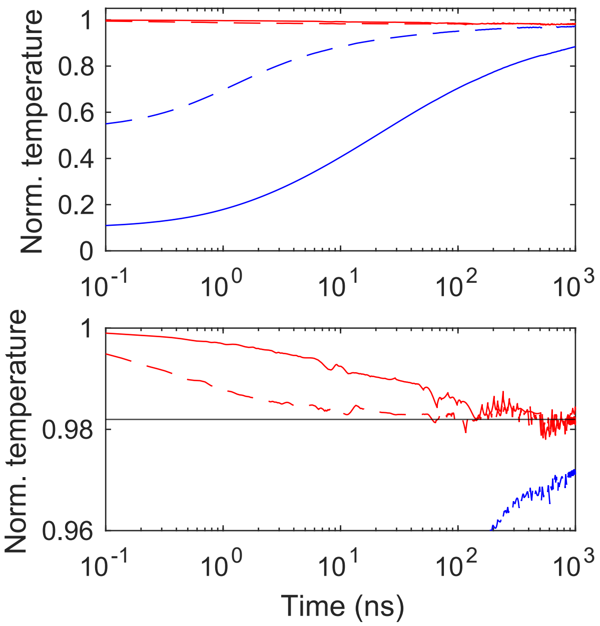

FIG. 7. Thermal diffusion simulations at a Sn-bond interface over the full range (a) and near the equilibrium temperature (b). Red lines show Sn temperatures and blue lines show glue temperatures. Boundary conductance is indicated by solid lines for 10^6 W/m^2·K and dashed lines for 10^7 W/m^2·K.

is 0.98, rather than 0.58, due to the much lower effusivity of glue compared to LiF. This estimate ignores the effects of glue compression, but plausible density increase (2×) and extreme conductivity increase (10×) only changes the equilibrium result to 0.92.

Figure 7 shows numerical simulations of a Sn-glue interface for several boundary conductance values. These plots are similar to Figure 3(c), with equilibrium much closer to the bulk Sn temperature. Lower boundary conductance (10^6–10^7 W/(m^2·K)) is considered because the glue is an amorphous insulator, so coupling with the metallic sample should be poorer than for LiF. The Sn surface gradually transitions from the initial bulk temperature, which is governed by the shock, release, reverberation sequence, to the equilibrium interface temperature; the latter is very close to the former in this geometry. Temperature measurements are governed by the Sn-glue interface, while mechanical measurements are largely unaffected by thin glue bonds. This disconnect results in observed stable thermal radiance during steady compression. A minor subtlety is that measurements must be compared with calculations that include the original shock, which is not directly observable in this geometry.

B. Direct-impact geometry

Direct-impact experiments accelerate the sample to a quasi-steady velocity before striking the stationary window, as shown in Figure 4(b). The window must be coated to block stray radiance from residual gas flash and other external sources. This coating must be simultaneously thin, opaque, fully dense, and not highly reflective; the last requirement is specific to optical pyrometry, *i.e.* good reflectors are poor emitters. Most paints and high-emissivity coatings are unsuitable for the dynamic compression thermometry. Porosity of any kind is prone to collapse at $\gg 1$ GPa, eliminating metal blacks[53] and surface texturing processes.[54] Paints are insufficiently opaque without 10–20 μm layers, which equilibrate too slowly to radiate at anything but their own intrinsic temperature; this is consistent with the observation similar radiance temperatures for such coatings placed on the sample and window sides of transmitted shock experiments.[55,56]

Pure graphite coatings must be $\gtrsim$280 nm thick for $>$ 99.9% opacity,[57] whereas a metal such as gold can attain similar opacity at less than 90 nm.[58] Quadratic scaling of diffusion time with thickness drives the need for the emission layer to be as thin as absolutely possible. However, additional thickness is usually needed to compensate for gradients in thickness across layers, reduce localized pinholes, and to provide optical densities well above 99.9% for mitigating strong impact flash. Thermal diffusivity favors metals over insulators, though emissivity can be an issue (particularly in the infrared). A two-layer metal coating, such as Cr covered with Au, can provide high emissivity ($\sim$50% or greater) and opacity at sub-micron thickness scales.

Figure 8(a) illustrates the pressure-particle velocity trajectories for a 2.137 km/s impact of Sn onto an Au-coated LiF window. The high mechanical impedance of the coating changes the reverberation path, subjecting to sample to a 51.7 GPa initial shock state. The sample undergoes several releases while the window compresses, eventually reaching a 23.6 GPa equilibrium. Figure 8(b) shows the pressure history just inside the Sn sample.

Although this direct-impact example leads to a similar pressure state as the transmitted-shock example discussed in Section III A: the simulated sample temperatures are quite different. Figure 9 compares temperature-pressure states for a Sn sample in both geometries. Reverse impact with the gold coating takes the Sn sample well above 2000 K, and isentropic release from this state brings the temperature down to about 1740 K. The transmitted-shock sample temperature ends up at around 1150 K.

The pressure histories in Figure 5(b) and Figure 8(b) do not propagate steadily into the Sn sample because the release waves propagate faster than the shock front.[1] Far from the interface, attenuation of the shock front by overtaking release waves washes out the effects of the glue/coating. Near the interface is a reverberation affected zone (RAZ) where loading history is very different than the bulk sample. Transmitted-shock experiments have a RAZ, but this hardly matters because the unloading and reverberation stages are nominally isen-

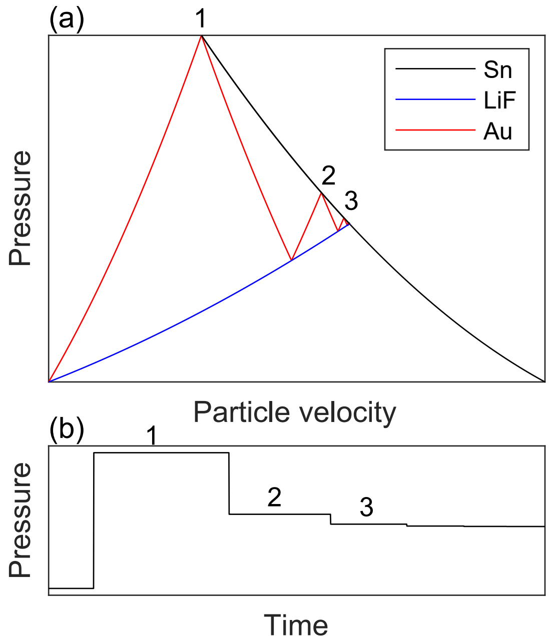

FIG. 8. (a) Calculated loading trajectory for a direct-impact experiment of Sn on Au-coated LiF. The black line indicates Sn shock states, the blue line indicates window shock states, and the red line indicates coating shock states. (b) Pressure history just inside the Sn sample. "1" represents the Sn shock pressure due to impact on Au, "2" and "3" the ring-down of the Au-LiF interface to the Sn-LiF impedance matched state.

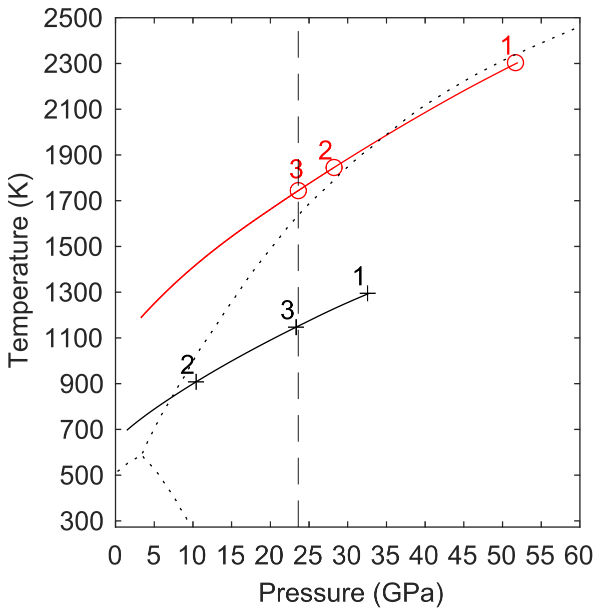

FIG. 9. Temperature-pressure states for transmitted-shock (black) and direct-impact (red) for a Sn sample, overlaid on the Sn phase diagram (dashed curves). The vertical dashed line indicates the final reverberation pressure in both geometries.

tropic. The direct-impact RAZ, however, is significantly hotter than the bulk sample as shown in Figure 9.

RAZ size is determined by the coating thickness h_c and wave speeds in the sample/coating. The initial sample shock propagates undisturbed during the first round trip coating transit; release waves from the LiF window must then overtake that shock. Assuming comparable shock speeds in the sample and coating, the RAZ thickness is:

$$h_{RAZ} \approx 2h_c \left[1 - \left(\sqrt{\frac{1+s\mu}{1-s\mu}}(1-\mu)+\mu\right)^{-1}\right]^{-1} \qquad (7)$$

for a linear material[59] ($U_s = c_0 + su_p$) compressed to $\mu \equiv 1 - \rho_0/\rho$. The Sn sample ($s \approx 1.5$) in the direct-impact described above has an initial compression of 31%; for comparison, Sn is compressed by 22% in the absence of gold. The RAZ must be at least 8× thicker than emissive coating, with some additional material needed for complete overtake of the release wave. The RAZ heat profile as a function of depth can also be modeled numerically with a hydrodynamics code.

Figure 10(a) illustrates how a 5 μm RAZ (compatible with a 500 nm Au coating) affects thermal diffusion in a direct-impact experiment. This simulation starts the RAZ at temperature state 1 and the bulk Sn at temperature state 3 as described in Figure 9. Infinite boundary conductance is assumed between the Sn-RAZ and RAZ-gold interfaces, but the Au-LiF interface is assigned $G = 10^8$ W/(m^2·K). Temperature snapshots indicate that excess heating in the RAZ diffuses into the sample and window, eventually creating a continuous profile that qualitatively matches snapshots in Figure 3.

Figure 10(b) compares Sn interface temperatures for different levels of Au-LiF conductance. After roughly 200 ns, differences between $G = 10^8$ W/(m^2·K) and $G = 10^9$ W/(m^2·K) are small but persist out to 1000 ns; the Sn interface remains significantly hotter for $G = 10^7$ W/(m^2·K). While all three temperature histories have a similar shape at later times, none of them converge to the 0.58 equilibrium state of a Sn-LiF interface. Excess heating of the RAZ makes the interface systematically hotter than a Sn-LiF interface, yet cooler than the Sn material away from the interface, at all times.

IV. EXPERIMENTAL METHODS AND RESULTS

Transmitted-shock and direct-impact experiments were performed with a smoothbore powder gun. In each experiment, a bare optical fiber probe collected light from the center of the measurement interface. A second probe transmitted laser light to the sample and collected reflection for a Photonic Doppler Velocimetry (PDV) interface velocity measurement.[24] Radiance signals were transmitted through low-OH multimode optical fibers and sent to two different multi-wavelength optical pyrometers which collected and quantified radiance across the near-infrared and visible spectrum. Spectral radiance was calculated

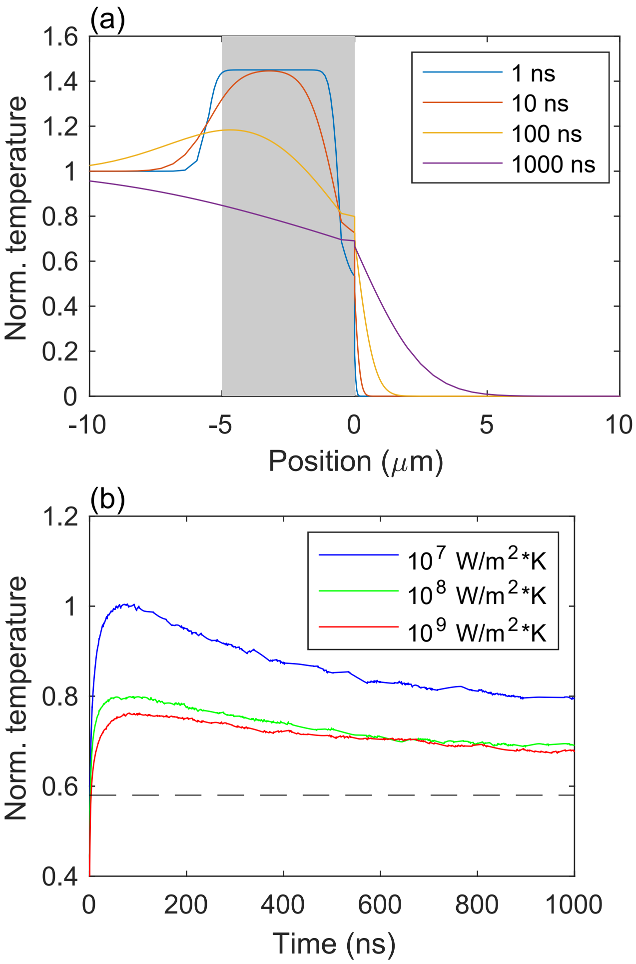

FIG. 10. (a) Temperature snapshots for thermal diffusion simulations of a Sn sample impacting a coated LiF window. Gray shading indicates a 5 μm RAZ that is hotter than the bulk Sn sample. A boundary conductance of 10^8 W/(m^2·K) is assumed between the gold coating and the LiF window. (b) Temperature histories for the Sn interface for different Au-LiF conductance. The dashed line indicates equilibrium temperature without the RAZ.

by comparison of measured photodetector voltages to signal levels measured across a wide range of radiance quantities emitted by a reference blackbody standard. Using plausible emissivity constraints under shock for Sn (transmitted shock) and Cr, Al, or Sn (reverse impact), radiance measurements were converted to time-resolved temperature by calculating a high temperature bound from the lowest emissivity, a low temperature bound from the highest emissivity, and reporting the mean of the two values.

A. Shock-transmission pyrometry

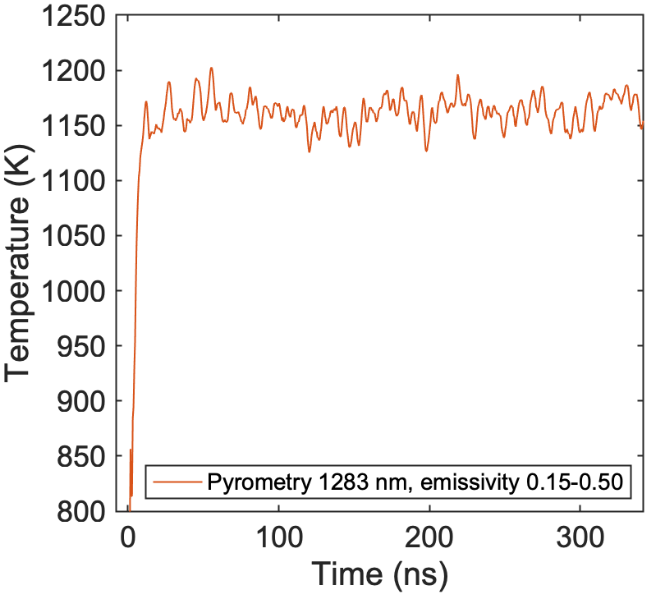

FIG. 11. Experimental interface temperature measurement for a transmitted-shock through Sn glued to LiF

Figure 11 shows temperature measurements for a transmitted-shock experiment with Sn glued to a LiF window. As discussed in Section III A, a Ta flyer generates a 33 GPa shock in Sn that ultimately releases to 23 GPa; the latter state is held until the arrival of the release wave from the back of the Ta flyer. During the steady loading phase (0–300+ ns) pyrometric temperature rises within detector response time and remains nearly constant, holding a mean value of 1162 K. No obvious temperature changes are observed for 300 ns after shock breakout, which is not surprising because the 2% temperature drop (normalized to the bulk sample-window difference) estimated from Equation 6 in Section III A would be less than 13 K.

Using a tabular equation of state[60] for Sn (Sesame 2160), the estimated bulk release-state temperature of Sn is ≈1150 K. This estimate is 25 K lower than diffusion-corrected pyrometry result for infinite boundary conductance and 12 K lower than the zero conductance case. This comparison is not a rigorous test of a particular equation of state, but rather an indication that while dynamic temperature uncertainties in glued-window experiments can approach 1–2%, uncertainties cannot be reduced significantly without further study of thermal properties under compression. Even with perfect radiance measurements and exact emissivity knowledge, associating an interface temperature with the bulk sample depends on some assumptions about diffusivity and interface conductance in the compressed state.

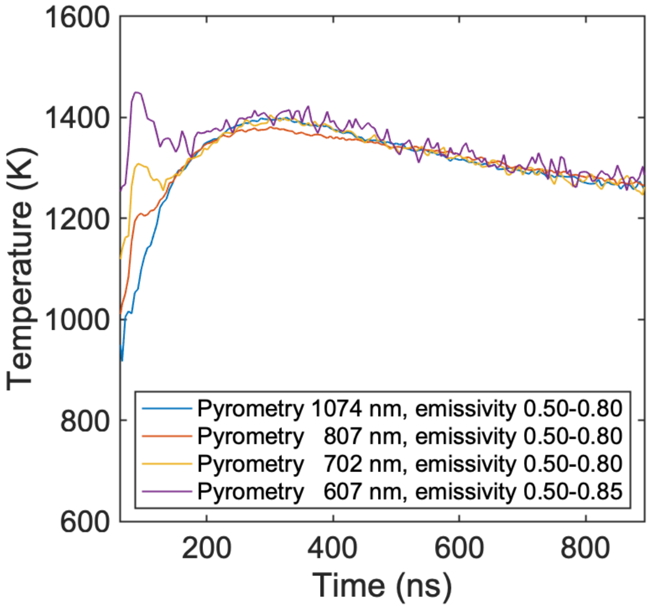

FIG. 12. Experimental interface temperature measurements for a direct impact of Sn on Au-Cr-coated LiF

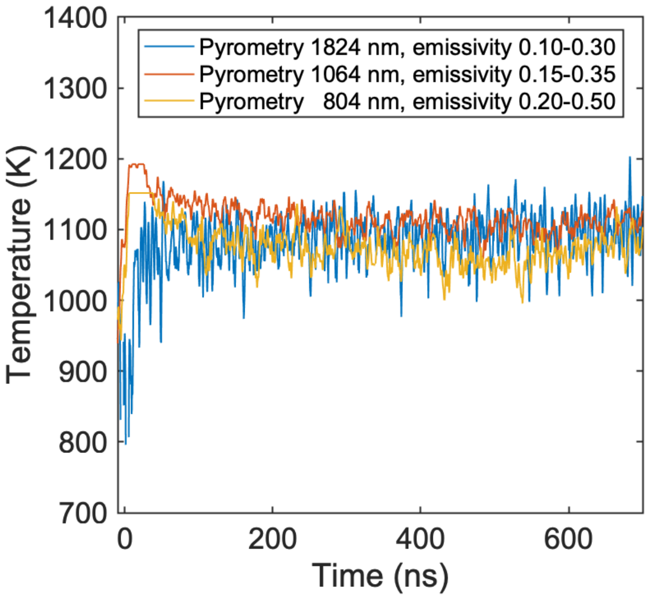

FIG. 13. Experimental interface measurements for a direct impact of Sn on Al/Cr-coated LiF

B. Direct-impact pyrometry

Figures 12–15 show temperature measurements from direct impact of Sn on coated LiF. Each experiment used an identical impactor with nearly identical impact velocity. The LiF windows were nominally identical as well; blinding/emissive window coatings were varied.

The first experiment (Figure 12) employed a LiF window coated with 500 nm of Cr and over-coated 500 nm of Au. This configuration screens nearly all light from the impact flash between projectile and target. After a small early-light flash at short wavelengths lasting ∼100 ns, consistent radiance profiles were obtained across a wide range of wavelengths shortly after shock breakout. Optical blinding by the Au overcoat was compromised by its high mechanical impedance, which creates a significant RAZ. As shown in Figure 9, the temperature of this zone is 2300 K while the bulk Sn temperature is closer to 1700 K. The 500 nm Cr coating between the Au layer and the LiF window further aggravates the excess heat issue. Chromium's high shock impedance relative to LiF generates additional over-pressure and heat, extending the RAZ depth, while also slowing diffusion of that heat due to its lower thermal diffusivity. We observed this excess RAZ heat diffusing away from the emitting Cr layer, but equilibrium was not achieved in the experiment.

Figure 13 shows temperature measurements from direct impact of Sn on LiF with a modified coating. The Cr layer was reduced to 10 nm and 500 nm of Al was used instead of Au, a combination that also blocked stray light but did not create substantial overheating. The apparent lack of a RAZ is due to the close impedance match between Al and LiF, as well as the reduction of Cr (which has higher impedance than LiF) from 500 nm to 10 nm. The primary function of the Cr layer is to lower Fresnel reflection at the LiF interface, which is achieved at ∼ 10 nm thickness; overcoat adhesion is a secondary benefit that does not require Cr layers ≫10 nm. Based on the pyrometry results and the conceptual framework from Section III B, this Cr-Al coating is suitable for direct-impact measurements with optical pyrometry while Cr-Au is not.

Figure 14 shows temperature measurements from reverse-impact of Sn on LiF with a pure Al coating (no Cr layer), which are nearly identical in temperature to Figure 13. The lower emissivity of the Al (compared to Cr) reduced measured radiance, cutting near-infrared signal in half. Absolute emissivity uncertainty creates proportionally greater temperature uncertainty as emissivity decreases. The worst case temperature uncertainty, calculated from radiance at 1064 nm, increased from ∼75 K in the Al-Cr coating to ∼110 K in the Al coating. While this simple coating is suitable for direct-impact measurements from a thermal diffusion perspective it is difficult pyrometrically. The Al-only coating also transmitted more background light—visible in the 804 nm temperature trace at ∼300 ns—likely due to the greater difficulty in producing quality coatings without the Cr layer.

Figure 15 shows another variation for the direct impact of Sn on LiF. In this case, the window was coated with 1000 nm of Sn for impact symmetry. The poor opacity of the Sn coating is apparent in the pyrometry data. Impact flash becomes visible at least 100 ns before impact at t=0 and saturates all but one radiance detec-

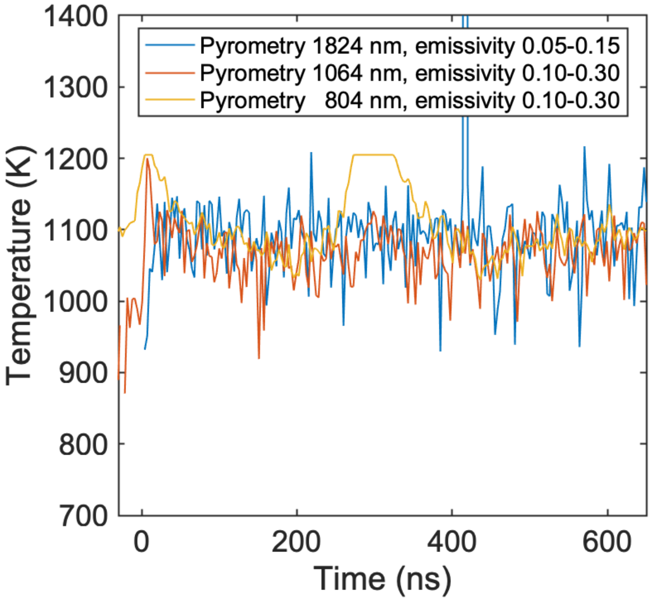

FIG. 14. Experimental interface temperature measurements for direct impact of Sn onto Al-coated LiF with no Cr layer.

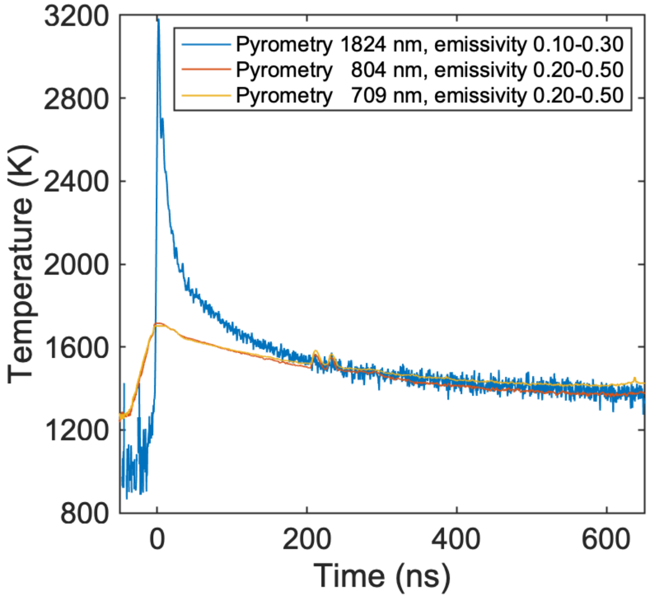

FIG. 15. Experimental interface temperature measurements for a symmetric direct-impact of Sn on Sn-coated LiF

tor. About 300 ns after breakout, the impact flash decays sufficiently for radiances to indicate a consistent interface temperature across different wavelengths. Much like the Au-overcoat, the high-impedance of the Sn coating (relative to LiF) creates a substantial RAZ that dominates interface temperature. This initial localized heating and subsequent cooling through the end of the measurement negates the benefits of symmetric impact. This coating is also unsuitable for direct impact pyrometry.

The optimal coating for a direct-impact experiment is a subtle compromise between emissivity, opacity, thermal diffusion, and impedance matching. Masking the sample's optical properties is a general benefit for coatings, *i.e.* highly reflective materials can be studied with optical pyrometry. An unfortunate side effect, however, is that interface temperatures would be systematically lower as direct sample contact with the window draws heat from the sample.

V. SUMMARY AND RECOMMENDATIONS

Material interfaces play an integral role in time-resolved temperature measurements, and for dynamic compression at least one of those interfaces is an optical window. Direct contact between a sample of interest and this window is conceptually simple, but in practice very difficult to achieve. Experiment geometries suitable for dynamic pyrometry measurements—transmitted shock and reverse impact—involve at least two thermal interfaces. The former relies on a transparent coupling between the sample and window, while the latter depends on an emissive window coating.

Glue/epoxy decomposition is the primary obstacle for transmitted-shock experiments: at high enough stresses, the coupling layer will become opaque and/or emitting. Low mechanical impedance of these layers leads to a reverberating shock compression, however, resulting in lower bond-layer temperatures and reduced decomposition. Based on thermodynamics and previous pyrometry work, Loctite® 326 glue is suitable for windowed pyrometry measurements to at least 50 GPa, though failure is likely well below 100 GPa. Within the glue's working range, transmitted-shock experiments benefit from low thermal diffusivity (and probably low boundary conductance), which keep the sample interface temperature very close to the bulk temperature for glue bonds >1 μm. This allows interface temperatures, accessible to pyrometry, of 0.98 of the bulk sample temperature of interest for time scales of 100-1000 ns. Even under the worst assumptions, interface temperatures likely hold at 0.92 of the bulk temperature. These values are relative to the difference between glue and sample. Absolute temperature uncertainty is somewhat smaller in nearly all cases. (*E.g.*, 0.98 of an 1150 K Sn sample in contact with a 720 K glue bond is 0.99 of the true 1150 K sample temperature.) Experiments show that temperatures in glued-window experiments rapidly equilibrate to steady values that plausibly agree with bulk sample temperature estimates. For glue-bonded experiments then, error in inferred bulk material temperature due to interface effects is generally smaller than, or similar to, experimental pyrometric error. For most dynamic studies cited in this work, uncertainty in dynamic spectral emissivity, background light, and other factors limit uncertainty to ∼2-10%.

Shielding/emissive coatings are the primary obstacle for direct-impact experiments. Even for 100 nm scale layers, coatings with higher mechanical impedance than the window (almost always LiF) create a RAZ at the sample interface. This zone is systematically hotter than the bulk sample, and thermal diffusion cannot sufficiently cool the interface within the duration of most impact experiments. Aluminum is a close shock impedance match with LiF, and experiments demonstrate that combining Al with a small Cr layer can yield stable emission very quickly. The disadvantage of this approach is that the interface temperature is now systematically lower than the bulk sample due to heat conduction into the (much cooler) window. This result also casts doubt on the advantages of direct sample-window single-interface measurements. Here too the measured thermal interface will differ from the bulk temperature of the shocked material. However, the greater difference between interface and bulk sample temperature requires greater assumptions with greater resultant uncertainty to calculate bulk sample temperature. For direct impact studies, experimental pyrometric error in the measured interface temperature will generally be smaller and easier to determine than the uncertainty due to thermal diffusion. Uncertainty in bulk temperature inferred from this interface temperature may be as high as ∼10–20% due to uncertainties in thermal properties of the interface materials under compression. While direct impact experiments conducted in this manner may yield high quality interface temperature measurements, future study is needed to relate the precise interface temperature back to the desired bulk sample temperature.

Interpreting dynamic temperature measurements is an ongoing challenge. At minimum, the association of a temperature with a particular state does not solely depend on equilibrium pressure. The path taken to equilibrium by the sample material—shock, release, reverberation versus shock, release(s)—is a significant factor; unfortunately, such information may not be evident in accompanying velocimetry measurements. Regrettably, temperature interpretation is not distinct from transport and interface properties, which are less well-known than the temperature itself. Clever experiments are needed to characterize transport and interface properties under dynamic compression.

ACKNOWLEDGMENTS

We would like to thank Kevin Baldwin for his work producing coatings; Carl Carlson, Bob Corrow, Erik Haroz, Cliff Cochran, and Adam Iverson for their work fielding pyrometry; and Mike Grover, Ben Valencia, and Matt Staska for their work fabricating and assembling the experimental targets.

Los Alamos National Laboratory is operated by Triad National Security, LLC for the National Nuclear Security Administration of U.S. Department of Energy under contract 89233218CNA000001.

Nevada National Security Site is operated by Mission Support and Test Services, LLC for the National Nuclear Security Administration of U.S. Department of Energy under contract DE-NA0003624. DOE/NV/03624--0790

Sandia National Laboratories is a multi-mission laboratory managed and operated by National Technology and Engineering Solutions of Sandia LLC, a wholly owned subsidiary of Honeywell International Inc. for the U.S. Department of Energy's National Nuclear Security Administration under contract DE-NA0003525.

This paper describes objective technical results and analysis. Any subjective views or opinions that might be expressed in the paper do not necessarily represent the views of the U.S. Department of Energy or the United States Government.

Data Availability: the data that support the findings of this study are available from the corresponding author upon reasonable request.

[1] G. Duvall and R. Graham, "Phase transitions under shock wave loading," Reviews of Modern Physics **49**, 523 (1977).

[2] S. Kormer, M. Sinitsyn, G. Kirillov, and V. Urlin, "Experimental determination of temperature in shock-compressed NaCl," Soviet physics JETP **21** (1965).

[3] G. Lyzenga and T. J. Ahrens, "Multiwavelength optical pyrometer for shock compression experiments," Review of Scientific Instruments **50**, 1421–1424 (1979).

[4] D. Partouche-Sebban, D. Holtkamp, J. Pélissier, J. Taboury, and A. Rouyer, "An investigation of shock induced temperature rise and melting of bismuth using high-speed optical pyrometry," Shock Waves **11**, 385–392 (2002).

[5] A. Seifter and A. W. Obst, "About the proper wavelength for pyrometry on shock physics experiments," International Journal of Thermophysics **28**, 934–946 (2007).

[6] W. Turley, G. Stevens, G. Capelle, M. Grover, D. Holtkamp, B. LaLone, and L. R. Veeser, "Luminescence from edge fracture in shocked lithium fluoride crystals," Journal of Applied Physics **113**, 133506 (2013).

[7] P. Coates, "Multi-wavelength pyrometry," Metrologia **17**, 103 (1981).

[8] A. Seifter, M. Grover, D. Holtkamp, A. Iverson, G. Stevens, W. Turley, L. Veeser, M. Wilke, and J. Young, "Emissivity measurements of shocked tin using a multi-wavelength integrating sphere," Journal of Applied Physics **110**, 093508 (2011).

[9] W. Turley, D. Holtkamp, L. Veeser, G. Stevens, B. Marshall, A. Seifter, R. Corrow, J. Stone, J. Young, and M. Grover, "Infrared emissivity of tin upon release of a 25 GPa shock into a lithium fluoride window," Journal of Applied Physics **110**, 103510 (2011).

[10] T. M. Hartsfield, A. J. Iverson, and J. Baldwin, "Reflectance determination of optical spectral emissivity of metal surfaces at ambient conditions," Journal of Applied Physics **124**, 105107 (2018).

[11] T. A. Ota, R. Amott, C. Carlson, D. J. Chapman, M. A. Collinson, R. Corrow, D. E. Eakins, T. Graves, T. Hartsfield, D. B. Holtkamp, *et al.*, "Comparison of simultaneous shock temperature measurements from three different pyrometry systems," Journal of Dynamic Behavior of Materials **5**, 396–408 (2019).

[12] G. Lyzenga, T. J. Ahrens, W. Nellis, and A. Mitchell, "The temperature of shock-compressed water," The Journal of Chemical Physics **76**, 6282–6286 (1982).

[13] W. Nellis, F. H. Ree, R. Trainor, A. Mitchell, and M. Boslough, "Equation of state and optical luminosity of benzene, polybutene, and polyethylene shocked to 210 GPa (2.1 Mbar)," The Journal of chemical physics **80**, 2789–2799 (1984).

[14] S.-N. Luo, J. A. Akins, T. J. Ahrens, and P. D. Asimow, "Shock-compressed $MgSiO_3$ glass, enstatite, olivine, and quartz: Optical emission, temperatures, and melting," Journal of Geophysical Research: Solid Earth **109** (2004).

[15] M. Boslough, "A model for time dependence in shock-induced thermal radiation of light," Journal of Applied Physics **58**, 3394 (1985).

[16] M. Mondot, *La température des matériaux soumis à une onde de choc*, Ph.D. thesis, Paris, CNAM (1993).

[17] A. Seifter, M. Grover, D. Holtkamp, J. Payton, P. Rodriguez, W. D. Turley, and A. Obst, "Low-temperature measurements on shock-loaded tin," in *26th International Congress on High-Speed Photography and Photonics*, Vol. 5580 (International Society for Optics and Photonics, 2005) pp. 93–105.

[18] S. Stewart, G. Kennedy, L. Senft, M. Furlanetto, A. Obst, J. Payton, and A. Seifter, "Post-shock temperature and free surface velocity measurements of basalt," in *AIP Conference Proceedings*, Vol. 845 (American Institute of Physics, 2006) pp. 1484–1487.

[19] A. Seifter, M. Furlanetto, M. Grover, D. Holtkamp, G. Macrum, A. Obst, J. Payton, J. Stone, G. Stevens, D. Swift, *et al.*, "Use of IR pyrometry to measure free-surface temperatures of partially melted tin as a function of shock pressure," Journal of Applied Physics **105**, 123526 (2009).

[20] W. T. Buttler, S. K. Lamoreaux, R. K. Schulze, J. D. Schwarzkopf, J. C. Cooley, M. Grover, J. E. Hammerberg, B. M. La Lone, A. Llobet, R. Manzanares, J. Martinez, D. Schmidt, D. Sheppard, G. Stevens, W. Turley, and L. Veeser, "Ejecta transport, breakup and conversion," Journal of Dynamic Behavior of Materials **3**, 334–345 (2017).

[21] J. D. Bass, B. Svendsen, and T. J. Ahrens, "The temperature of shock compressed iron," High Pressure Research in Mineral Physics **39**, 393–402 (1987).

[22] W. Nellis and C. Yoo, "Issues concerning shock temperature measurements of iron and other metals," Journal of Geophysical Research **95**, 21749–21752 (1990).

[23] L.M. Barker and R.E. Hollenbach, "Laser interferometer for measuring high velocities of any reflecting surface," Journal of Applied Physics **43**, 4669–4675 (1972).

[24] O. Strand, D. Goosman, C. Martinez, T. Whitworth, and W. Kuhlow, "Compact system for high-speed velocimetry using heterodyne techniques," Review of Scientific Instruments **77**, 83108 (2006).

[25] P. Urtiew and R. Grover, "Temperature deposition caused by shock interactions with material interfaces," Journal of Applied Physics **45**, 140 (1974).

[26] R. Grover and P. Urtiew, "Thermal relaxation at interfaces following shock compression," Journal of Applied Physics **45**, 146 (1974).

[27] H. Carslaw and J. Jaeger, *Conduction of heat in solids*, 2nd ed. (Oxford University Press, Oxford, 1959).

[28] A. Salazar, "On thermal diffusivity," European Journal of Physics **24**, 351 (2003).

[29] Y. S. Touloukian, R. Powell, C. Ho, and M. Nicolaou, "Thermophysical Properties of Matter-The TPRC Data Series. Volume 10. Thermal Diffusivity," Tech. Rep. (Thermophysical and Electronic Properties Information Analysis Center . . . , 1974).

[30] W. Schiesser and G. Griffiths, *A compendium of partial differential equation models: method of lines analysis with MATLAB* (Cambridge University Press, 2009).

[31] R. Jacobs and C. Starr, "Thermal conductance of metallic contacts," Review of Scientific Instruments **10**, 140 (1939).

[32] A. Tariq and M. Asif, "Experimental investigation of thermal contact conductance for nominally flat metallic contact," Heat and Mass Transfer **52**, 291 (2016).

[33] P. Hopkins, "Thermal transport across solid interfaces with nanoscale imperfections: effects of roughness, disorder, dislocations, and bonding on thermal boundary conductance," ISRN Mechanical Engineering **2013**, 682586 (2013).

[34] G. Hohensee, R. Wilson, and D. Cahill, "Thermal conductance of metal–diamond interfaces at high pressure," Nature Communications **6**, 6578 (2015).

[35] C. Yoo, N. Holmes, M. Ross, D. Webb, and C. Pike, "Shock temperatures and melting of iron at Earth core conditions," Physical Reviews Letters **70**, 3931 (1993).

[36] J. H. Nguyen and N. C. Holmes, "Melting of iron at the physical conditions of the earth's core," Nature **427**, 339–342 (2004).

[37] O. Anderson, "Physics of iron," Tech. Rep. (Lawrence Livermore National Lab., CA (United States), 1993).

[38] O. L. Anderson and A. Duba, "Experimental melting curve of iron revisited," Journal of Geophysical Research: Solid Earth **102**, 22659–22669 (1997).

[39] M. J. Brown, "The equation of state of iron to 450 GPa: Another high pressure solid phase?" Geophysical Research Letters **28**, 4339–4342 (2001).

[40] D. Hare, N. Holmes, and D. Webb, "Shock-wave-induced optical emission from sapphire in the stress range 12 to 45 GPa: Images and spectra," Physical Review B **66**, 014108 (2002).

[41] D. Partouche-Sebban, J. Pelissier, W. Anderson, R. Hixson, and D. Holtkamp, "Investigation of shock-induced light from sapphire for use in pyrometry studies," Physica B: Condensed Matter **364**, 1–13 (2005).

[42] J. Winey, M. Knudson, and Y. Gupta, "Shock compression response of diamond single crystals at multimegabar stresses," Physical Review B **101**, 184105 (2020).

[43] K. Katagiri, N. Ozaki, K. Miyanishi, N. Kamimura, Y. Umeda, T. Sano, T. Sekine, and R. Kodama, "Optical properties of shock-compressed diamond up to 550 GPa," Physical Review B **101**, 184106 (2020).

[44] K.-i. Kondo, T. J. Ahrens, and A. Sawaoka, "Shock-induced radiation spectra of fused quartz," Journal of applied physics **54**, 4382–4385 (1983).

[45] G. A. Lyzenga, T. J. Ahrens, and A. C. Mitchell, "Shock temperatures of sio2 and their geophysical implications," Journal of Geophysical Research: Solid Earth **88**, 2431–2444 (1983).

[46] P. Rigg, M. Knudson, R. Scharff, and R. Hixson, "Determining the refractive index of shocked [100] lithium fluoride to the limit of transmissibility," Journal of Applied Physics **116**, 033515 (2014).

[47] J. Wise and L. Chhabildas, "Shock waves in condensed matter," (1986).

[48] C. A. McCoy, M. D. Knudson, and M. P. Desjarlais, "Sound velocity, shear modulus, and shock melting of beryllium along the hugoniot," Physical Review B **100**, 054107 (2019).

[49] L. Kirsch, S. Ali, D. Fratanduono, R. Kraus, D. Braun, A. Fernandez-Pañella, R. Smith, J. McNaney, and J. Eggert, "Refractive index of lithium fluoride to 900 gigapascal and implications for dynamic equation of state measurements," Journal of Applied Physics **125**, 175901 (2019).

[50] D. Partouche-Sebban, J. Pélissier, F. Abeyta, W. Anderson, M. Byers, D. Dennis-Koller, J. Esparza, R. Hixson, D. Holtkamp, B. Jensen, *et al.*, "Measurement of the shock-heated melt curve of lead using pyrometry and reflectometry," Journal of applied physics **97**, 043521 (2005).

[51] M. Akin and R. Chau, "The suitability of Loctite 326 for thermal emission measurements," Journal of Dynamic Behavior of Materials **2**, 421 (2016).

[52] D. Dattlebaum and J. Coe, "Shock-driven decomposition of polymers and polymeric foams," Polymers **11**, 493 (2019).

[53] P. O'Neill and A. Ignatiev, "Influence of microstructure on the optical properties of particulate materials: gold black," Physical Review B **18**, 6540 (1978).

[54] A. Vorobyev, V. Makin, and C. Guo, "Brighter light sources from black metal: significant increase in emission efficiency of incandescent light sources," Physical Review Letters **102**, 234301 (2009).

[55] C. Chauvin, J. Petit, P. Héreil, and M. Boustie, "Analysis of temperature measurement at material/LiF interface under moderate shock wave compression," in *DYMAT-International Conference on the Mechanical and Physical Behaviour of Materials under Dynamic Loading*, Vol. 1 (EDP Sciences, 2009) pp. 311–317.

[56] C. Chauvin, J. Petit, and F. Sinatti, "An application of the emissive layer technique to temperature measurement by infrared optical pyrometer," in *AIP Conference Proceedings*, Vol. 1426 (American Institute of Physics, 2012) pp. 368–371.

[57] A. Djurisic and E. Li, "Optical properties of graphite," Journal of Applied Physics **85**, 7404 (1999).

[58] P.B. Johnson and R.W. Christy, "Optical constants of the noble metals," Physical Review B **6**, 4370 (1972).

[59] M. Rice, R. G. McQueen, and J. Walsh, "Compression of solids by strong shock waves," Solid State Physics **6**, 1–63 (1958).

[60] "Sesame: the Los Alamos National Laboratory equation of state database," Tech. Rep. LA-UR-3407 (Los Alamos National Laboratory, 1992).

[61] J. McGlaum and S. Thompson, "CTH: a three-dimensional shock wave physics code," International Journal of Impact Engineering **10**, 351 (1990).

[62] S. Thomas, L. Veeser, W. Turley, and R. Hixson, "Comparisons of CTH simulations with measured wave profiles for simple flyer plate experiments," Journal of Dynamic Behavior of Materials **2**, 365 (2016).

[63] J. VonNeumann and R. Richtmyer, "A method for the numerical simulation of hydrodynamic shocks," Journal of Applied Physics **21**, 232 (1950).

Appendix A: Numerical simulations

In principle, the temperature history of an emitting surface can be explicitly modeled. Given the appropriate material models, wave codes such as CTH[61] can reliably simulate mechanical states (density, stress, etc.) created by dynamic compression; subtle details, such as zone sizing, can be an issue.[62] Accurate temperature calculations are more difficult to obtain. Codes that handle shock compression do not typically include thermal diffusion (and vice versa), especially considering finite boundary conductance.

The artificial viscosity used by wave codes[63] also has a non-negligible impact on temperature. Each computational zone experiences a time-dependent strain based on the simulation design: impact velocity, sample thickness, and so forth. Temperature generally increases with adiabatic strain, but that increase also depends on strain rate: faster deformation produces more entropy (mimicking shock compression) while slower deformation produces less entropy (mimicking isentropic compression). Strain rate is implicitly tied to artificial viscosity settings (usually 1–2 adjustable parameters) and zone size (uniform or variable across each material layer). Zones near a material interface may observe a different strain rate than those deeper inside a material, even for steady shock propagation, due to changes in the simulated wave profile across the interface.

Detailed exploration of the computational temperature artifacts is beyond the scope of this work. The simulations discussed in Sections II and III assume instantaneous compression near the sample interface. The ratio κ/U_s^2 (where U_s is shock velocity) is a characteristic time scale when shock propagation overtakes thermal diffusion. Even in highly diffusive metals, this overtake occurs on 0.01 ns time scales, so it is reasonable to consider semi-infinite bulk temperatures for diffusion times $\gtrsim 0.1$ ns.

Isobaric diffusion after shock compression is treated here using the numerical method of lines.[30] Figure 16 illustrates a one-dimensional representation of this technique for a three-layer simulation. Each layer is divided into $m = 1..M$ zones, with the right-most zone of one layer at the same physical location as the left-most zone of the next layer. External boundary zones ($m = 1$ and $m = M$) are perfectly insulating, *i.e.* $\partial T/\partial x = 0$. Internal boundary zones ($m = 6$ and $m = 12$ in Figure 16) are subject to boundary conditions given by Equations 3–4. Standard thermal diffusion:

$$\frac{dT}{dt} = \kappa \frac{\partial^2 T}{\partial x^2}$$

occurs at all other zones. The finite difference representation of Equation A:

$$\frac{dT_m}{dt} \approx \frac{\kappa_m}{\Delta_m^2}\Big[T_{m+1} - 2T_m + T_{m-1}\Big] \tag{A1}$$

is accurate to third power of zone width Δ. Forward/backward differences of similar order applied to the boundary conditions to obtain analytic expressions for temperature at these locations. For example:

$$T_1 = \frac{18T_2 - 9T_3 + 2T_4}{11}$$
$$T_M = \frac{2T_{M-3} - 9T_{M-2} + 18T_{M-1}}{11}$$

are the external boundary temperatures accurate to $\mathcal{O}(\Delta^3)$.

Initial temperature distributions $T_m = T(x_m, t = 0)$ are determined from shock, multiple shock, and release states discussion in Sections II–III. Subsequent temperature profiles are determined by a sparsely-coupled ordinary differential equations (Equation A1). At each time step, including $t = 0$, internal and external boundary conditions are used to determine temperature at the locations where Equation A1 is not used. Stiff integrators are typically needed to maintain reasonable time steps. Increased computation speed is also obtained by dividing each material layer into 2–3 separate layers, with dense zoning near internal boundaries and coarse zoning everywhere else.

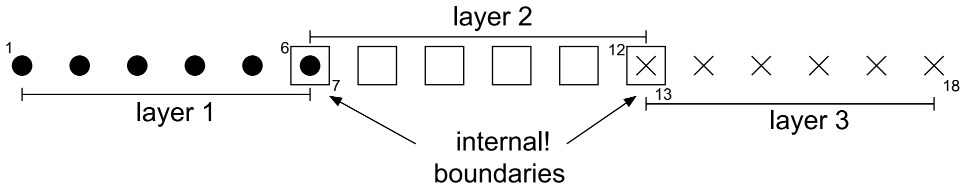

[t]

FIG. 16. Conceptual zone layout for isobaric thermal diffusion in a three-layer simulation ($M = 18$)